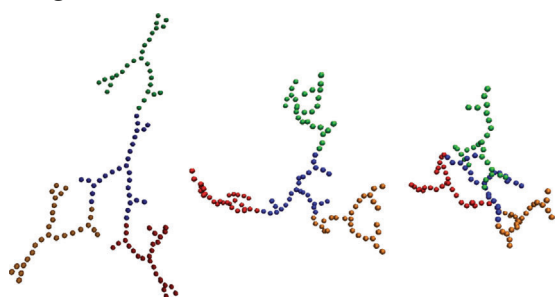


# Molecular Dynamics Simulations of Hyperbranched PAMAM Vicsek Fractals

Florian Fürstenberg,\* Andrey A. Gurtovenko, Maxim Dolgushev,  
Alexander Blumen

Within the broad class of hyperbranched polymers, highly symmetrical objects (such as dendrimers and Vicsek fractals) are of special theoretical interest. Here we study, using the MARTINI force-field, polyamidoamine Vicsek fractals (PVF) *in silico*, focusing on their structure and dynamics in dilute solution. Our extensive microsecond-long simulations show that the radius of gyration of PVF scales with the molecular weight as  $N^{0.54}$ , behavior rather close to that of stars and considerably distinct from that of dendrimers. The study of the radial density profiles indicates that different parts of the PVF interpenetrate significantly, fact which stresses the soft and sparse character of PVF. These results are also supported by our findings for the rotational autocorrelation functions.



## 1. Introduction

Recently, hyperbranched polymers gained a lot of interest, both theoretically and experimentally.<sup>[1,2]</sup> While hyperbranched polymers are a broad and highly colorful class of materials, with much freedom in their architecture, a special theoretical focus lies on highly symmetrical, regular patterns. Here in particular, *dendritic structures*<sup>[3–7]</sup> and *Vicsek fractals*<sup>[8–12]</sup> (VF) enjoy remarkable attention. Because of their symmetry these polymer classes allow to simplify analytical approaches, leading to a clear and detailed understanding of their behavior.<sup>[2,3,6,13–18]</sup> On the experimental side, dendrimers were extensively synthesized, while Vicsek fractals (VF) were not up to now. Dendrimers show a large variety of promising applications, ranging from catalysis<sup>[19]</sup> to biomedical delivery systems,<sup>[20]</sup> so that much effort was put in investigating them

through experiments<sup>[21–24]</sup> and computer modeling.<sup>[25–29]</sup> We note, however, that one of the major issues with dendrimers is the packing problem with increasing generation which, in fact, limits their growth. In contrast, the regular, hyperbranched structure of VF is considerably more sparse than that of dendrimers. In fact, due to their particular hierarchical construction, VF are not limited by packing issues in their growth.<sup>[9]</sup> Moreover, while the relaxation dynamics of dendrimers does not show typical scaling behavior, for VF many dynamical quantities scale as a function of their spectral dimension.<sup>[13]</sup> It is therefore of interest to investigate the properties of VF in spite of the fact that they presently do not exist as chemical compounds.

In this paper, we study polyamidoamine (PAMAM) Vicsek fractals (in short, PVF) *in silico* and employ extensive molecular dynamics simulations to determine their structural and dynamic properties. In doing that, we chose to use the MARTINI force-field,<sup>[30]</sup> an extensively validated coarse-grained model of near-atomistic resolution, which was recently adapted for describing hyperbranched PAMAM dendrimers (PD).<sup>[26,27]</sup> Overall, our simulations provide a detailed, near-atomistic insight into the structure and dynamics of PAMAM hyperbranched polymers that possess a Vicsek fractal topology. For the sake of comparison to related compounds all results are confronted with the corresponding findings for PD.

F. Fürstenberg, M. Dolgushev, A. Blumen  
Theoretical Polymer Physics, University of Freiburg, Hermann-Herder-Str. 3, D-79104 Freiburg, Germany  
E-mail: florian.fuerstenberg@physik.uni-freiburg.de  
A. A. Gurtovenko  
Institute of Macromolecular Compounds, Russian Academy of Sciences, Bolshoi pr. V.O. 31, St.Petersburg 199004 Russia  
Faculty of Physics, St.Petersburg State University, Ul'yanovskaya ul. 1, Petrodvorets, St.Petersburg 198504 Russia

The article is structured as follows: In the next section “*Model and Simulation Methods*” we summarize the architectural properties of Vicsek fractals and sketch the computational model used. Section “*Results and Discussion*” presents our findings as far as the structural and dynamic properties of PVF are concerned. Finally, we summarize our results in the last section “*Conclusions*.”

## 2. Model and Simulation Methods

### 2.1. PAMAM Vicsek Fractals

At first, we recall the hierarchical construction of the VF. VF were introduced in ref.<sup>[31]</sup> and their dynamical properties were theoretically analyzed in refs.<sup>[8–13]</sup> In general, VF are characterized by two parameters, namely by their functionality  $f$  (number of nearest neighbors of a branching point), and by their generation  $G$  (number of iterations performed in their creation), see Figure 1 which shows a VF of functionality  $f=3$  and generation  $G=3$ . Generation zero ( $G=0$ ) starts with a sole bead, which acts as the seed for the first iteration step in which 3 new beads are attached to it. In the second iteration step, the whole VF of generation  $G=1$  acts as a new seed to which now 3 other  $G=1$  VF are attached symmetrically, as shown in Figure 1. This procedure is then iterated. The central bead (corresponding to the  $G=0$  VF) is called *core*. We remark that the procedure highlighted here can be readily extended to VF of arbitrary functionality  $f$ .<sup>[9,13]</sup>

Here we study VF based on the MARTINI force-field used for PD.<sup>[26,27]</sup> Now for PD, each arm of the peripheral shell consists of a linear spacer connected to a branching point (belonging to the previous shell) and to one terminal bead, see Figure 2b. Hence we have to adapt the hierarchical

construction for VF accordingly: We start from a core consisting of a sole bead, to which now 3 arms of length 2 are attached (instead of 3 single beads), creating a VF architecture of generation  $G=1$ . The iteration works then as for the simple VF, with generation  $(G+1)$  of this VF architecture being built out of  $(3+1)$  structures of generation  $G$ , where one of them acts as the starting seed. We call the ensuing structures PAMAM VF (PVF) and denote a PVF of generation  $G$  by PVFG.

Now, Figure 2 shows schematically a PVF3 (Figure 2a) and a PD3 (Figure 2b). Beads belonging to the same shell  $g$  are color-coded. Here, shells follow naturally from the iteration procedure and contain the newly attached beads. The figure is only meant to display the connections between beads, i.e., the topology of the structure. The geometrical form of the structures presented may be quite different from these drawings, as we discuss in the following. From the figure is evident that a stretched PVF occupies by far less of its available space than a PD of the same functionality and generation. Moreover, because of its construction scheme, a PVF with  $f=3$  or  $f=4$  can be readily embedded in the three-dimensional space for any value of  $G$ .<sup>[9]</sup>

According to the presented hierarchical construction, a PVF1 consists of 7 beads. Following the scheme of a VF presented in Figure 1, a PVF2 consists of  $7 \times 4 = 28$  beads. Hence, a PVFG is built out of  $(7 \times 4^{G-1})$  beads. Counting the beads in a similar fashion as for PVF, a PDG is made of  $2 + 4 \times 2 \times \sum_{i=0}^G 2^i = 4 \times 2^{G+2} - 6$  beads. In particular, this means that a PVF3 and a PD3 contain comparable numbers (112 and 122) of beads, respectively. The same holds also for a PVF4 and a PD5. Moreover, from the hierarchical architecture of PVF and PD the degree of branching (DB)<sup>[32,33]</sup> follows readily; for PVF of generations  $G=2, 3$ , and  $4$  the DB is approximately 0.357, 0.304, and 0.290, tending toward 2/7 for large  $G$ , while for PD of generations

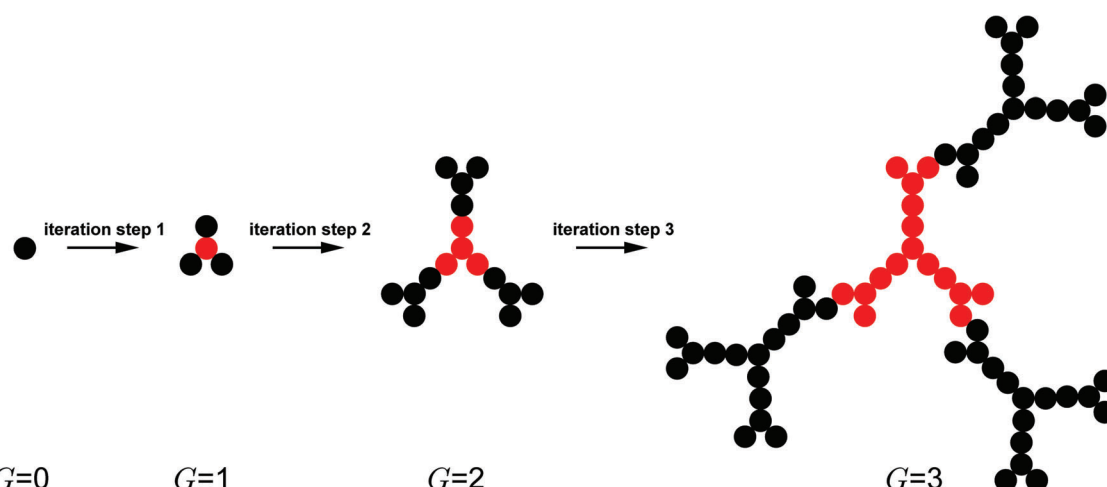


**Figure 1.** Iterative construction of a Vicsek fractal of functionality  $f=3$  and generation  $G=3$ . The particular seed of an iteration step is depicted in red, see text for details.

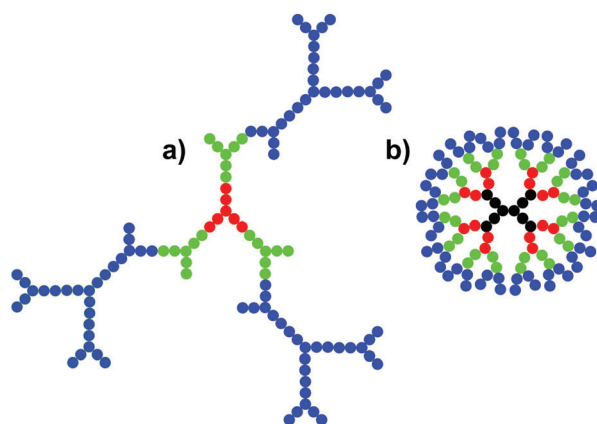


**Figure 2.** Illustration (a) of a coarse-grained PAMAM Vicsek fractal and (b) of a PAMAM dendrimer of functionality  $f=3$  and generation  $G=3$ . Beads belonging to the same shell  $g$  were colored in the same way:  $g=0$  in black,  $g=1$  in red,  $g=2$  in green, and finally  $g=3$  in blue.

$G = 2, 3, 4$ , and  $5$  the DB is approximately  $0.517, 0.508, 0.504$ , and  $0.502$ , tending toward  $1/2$  for  $G$  large.

## 2.2. Coarse-Grained Molecular Dynamics Simulations

We have performed molecular dynamics simulations of PVF in dilute solutions, for which the number of generations was varied from two to four. The initial structures of the generated hyperbranched polymers were solvated with a coarse-grained solvent, for which, depending on the system, the number of solvent particles varied from 3 164 to 1 051 943: In Table 1, we list the systems studied. Note that due to the very sparse and stretched structure of PVF, see Figure 2, we are forced, especially for PVF4, to use large boxes (able to contain an entire spread-out structure) in order to avoid any effects related to the boundaries. For the sake of comparison, we also performed MD simulations of PD of generations two to five.

All PVFs were simulated in the framework of the latest version of the coarse-grained MARTINI force-field adapted

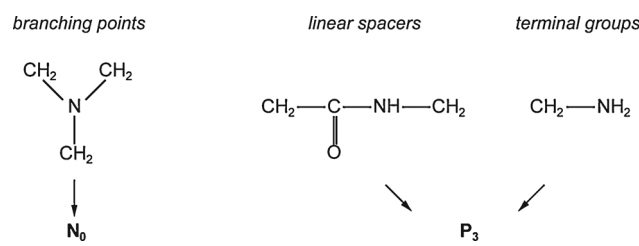


**Figure 3.** Mapping of the chemical structures of PAMAM Vicsek fractals into coarse-grained MARTINI beads.

for PD.<sup>[27]</sup> The corresponding coarse-grained (CG) beads are shown in Figure 3: The beads that represent branching points are called  $N_0$  and the beads related to linear spacers and to terminal groups are called  $P_3$ . These notations were introduced for the MARTINI force-field in ref.<sup>[30]</sup> and represent two different main categories:  $P$  indicates that the CG beads are polar while  $N$  denotes nonpolar beads. Furthermore, the indices differentiate among the subtypes.<sup>[30]</sup> The index of  $N$  is related to the hydrogen-bond capacities of the bead; here 0 stands for no hydrogen-bond capacities; for  $P$  the index refers to an increasing level of polarity and ranges from 1 to 5.<sup>[30]</sup> Here we use these CG beads for the *in silico* realization of VF structures. Figure 4 displays the coarse-graining procedure for a PVF2 together with the corresponding structural formulas of the two different chemical subunits (PVF1) which we envisage. Finally, for the simulation of water we used the standard MARTINI representation<sup>[27,30,34]</sup> which maps four water molecules to one CG bead of category  $P_4$ .

The non-bonded interactions between CG beads are modeled by Lennard-Jones potentials of the form

$$V_{ij}(r_{ij}) = C_{ij}^{(12)} / r_{ij}^{12} - C_{ij}^{(6)} / r_{ij}^6. \quad (1)$$

The parameters  $C_{ij}^{(6)}$  and  $C_{ij}^{(12)}$  for all non-bonded interactions were originally developed by Marrink et al.<sup>[30]</sup> For the  $P_3-P_4$  interactions the original MARTINI values are  $C^{(12)} = 0.23238 \times 10^{-2} \text{ kJ} \cdot \text{nm}^{12} \cdot \text{mol}^{-1}$  and

**Table 1.** Simulated polymer systems.

System	Architecture	Generation	Number of polymer beads	Number of solvent beads
PVF2	Vicsek fractal	2	28	3 164
PVF3	Vicsek fractal	3	112	38 215
PVF4	Vicsek fractal	4	448	1 051 943
PD2	dendrimer	2	58	1 177
PD3	dendrimer	3	122	2 329
PD4	dendrimer	4	250	4 811
PD5	dendrimer	5	506	9 686

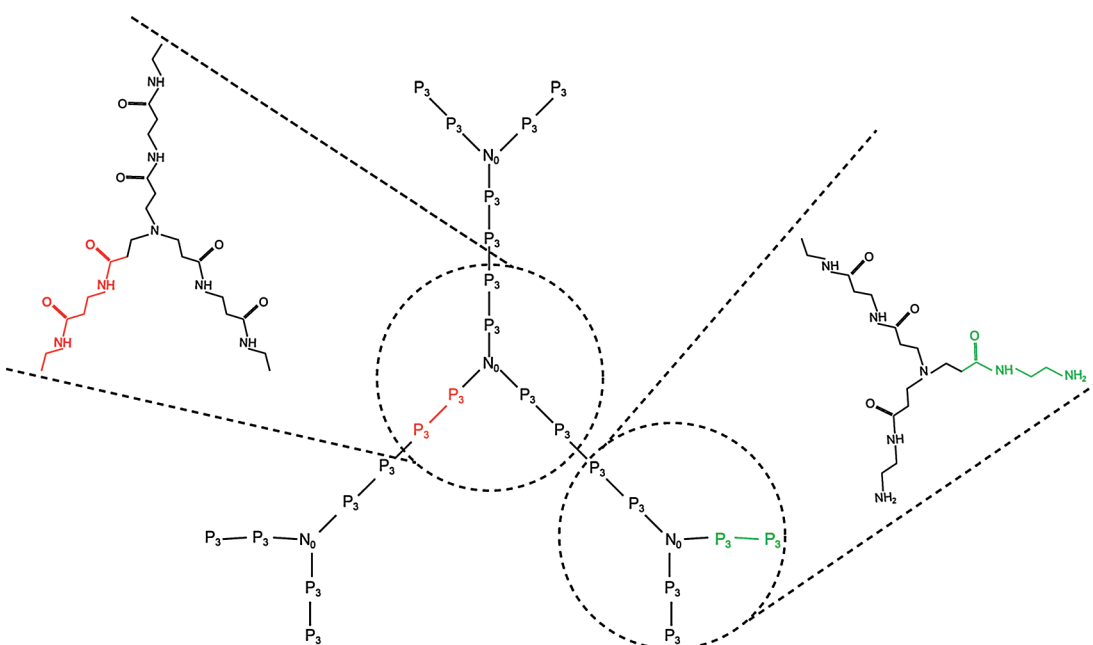


**Figure 4.** Sketch of a coarse-grained PVF of generation  $G=2$ . The corresponding structural formulas of the two different subunits (PVF of generation  $G=1$ ) are shown between the dashed lines.

$C^{(6)} = 0.21558 \text{ kJ} \cdot \text{nm}^6 \cdot \text{mol}^{-1}$ . These parameters were adapted to PD by Lee and Larson in ref.,<sup>[27]</sup> and were set to  $C^{(12)} = 0.23703 \times 10^{-2} \text{ kJ} \cdot \text{nm}^{12} \cdot \text{mol}^{-1}$  and  $C^{(6)} = 0.21990 \text{ kJ} \cdot \text{nm}^6 \cdot \text{mol}^{-1}$ , respectively, a choice which we adopt in the following. We list all non-bonded interactions parameters used by us in Table 2.

In turn, bonded interactions between nearest (NN) and next-nearest neighboring (NNN) beads are modeled through weak harmonic potentials<sup>[35]</sup>

$$V_{\text{NN}}(d) = \frac{1}{2} K_{\text{bond}} (d - l_{\text{eq}})^2 \quad (2)$$

and weak harmonic angle potentials<sup>[35]</sup>

$$V_{\text{NNN}}(\theta) = \frac{1}{2} K_{\text{angle}} (\theta - \theta_{\text{eq}})^2. \quad (3)$$

In Equation (2) and (3) we follow Lee and Larson<sup>[27]</sup> and use their parameters, listed in Table 3.

According to the standard MARTINI parameterization,<sup>[30]</sup> the Lennard-Jones interactions were cut off at 1.2 nm with a shift to 0 in the range 0.9–1.2 nm. All systems were

simulated in the  $NpT$ -ensemble at a temperature of 310 K with the pressure being set to 1 bar. Both temperature and pressure were kept constant by the Berendsen scheme.<sup>[36]</sup> The particular PVF and the solvent were independently coupled to the thermostat with a coupling constant  $\tau_T$  of 1 ps. The corresponding coupling constant  $\tau_P$  of the barostat was set to 3 ps. The time step was set to 20 fs. Each system was simulated for 1  $\mu$ s, the initial part of the trajectory (defined individually for each simulated system type) was viewed as an equilibration period and discarded from the subsequent analysis. The simulation package GROMACS-4.5.5 was used in all simulations.<sup>[35]</sup>

## 3. Results and Discussion

### 3.1. Radii of Gyration

At first, we determined the radii of gyration  $R_g$  for all the PVF structures considered ( $G=2$ , 3, and 4). Now, for each polymer,  $R_g$  is given by the root mean square distance of its parts from its center of mass (COM) and can be calculated

**Table 2.** Lennard-Jones parameters used for all simulations of PD and PVF chosen as in refs.<sup>[27,30]</sup> Here  $C^{(6)}$  and  $C^{(12)}$  are given in units of  $\text{kJ} \cdot \text{nm}^6 \cdot \text{mol}^{-1}$  and  $10^{-2} \text{ kJ} \cdot \text{nm}^{12} \cdot \text{mol}^{-1}$ , respectively.

	$\mathbf{N}_0-\mathbf{N}_0^{[30]}$	$\mathbf{N}_0-\mathbf{P}_3^{[30]}$	$\mathbf{N}_0-\mathbf{P}_4^{[30]}$	$\mathbf{P}_3-\mathbf{P}_3^{[30]}$	$\mathbf{P}_3-\mathbf{P}_4^{[27]}$	$\mathbf{P}_4-\mathbf{P}_4^{[30]}$
$C^{(6)}$	0.15091	0.15091	0.15091	0.21558	0.21990	0.21558
$C^{(12)}$	0.16267	0.16267	0.16267	0.23238	0.23703	0.23238

**Table 3.** Parameters of bonded interactions used for all simulations of PVF and PD chosen as in refs.<sup>[27]</sup> Here  $K_{\text{bond}}$  and  $K_{\text{angle}}$  are given in units of  $\text{kJ} \cdot \text{nm}^{-2} \cdot \text{mol}^{-1}$  or  $\text{kJ} \cdot \text{rad}^{-2} \cdot \text{mol}^{-1}$ , respectively,  $l_{\text{eq}}$  in nm and  $\theta_{\text{eq}}$  in degrees ( $^\circ$ ), respectively.

$V_{\text{NN}}$		$V_{\text{NNN}}$		
		Branching bead	Linear spacer	
$K_{\text{bond}}$	4000	$K_{\text{angle}}$	20	70
$l_{\text{eq}}$	0.42	$\theta_{\text{eq}}$	120	160

directly from the MD trajectories through:

$$R_g = \left( \frac{\sum_i m_i |\mathbf{r}_i|^2}{\sum_i m_i} \right)^{\frac{1}{2}}. \quad (4)$$

Here  $m_i$  denotes the mass of bead  $i$  and  $\mathbf{r}_i$  is its position vector with respect to the COM. Note, that the particular values of  $m_i$  are defined by the MARTINI force field<sup>[30]</sup> and that they are set to 72 amu for all beads.

In Figure 5, we present the time development of  $R_g$  for the simulated PVF ( $G = 2, 3$ , and  $4$ ) calculated using Equation (4). All the simulations started from almost stretched PVF (i.e., the realizations shown in Figure 2 and 4) solvated in coarse-grained water. It turned out that for PVF2 the initial  $R_g$  is relatively close to its equilibrium value, see Figure 5. In contrast, the behavior of PVF3 and PVF4 is quite different: In the course of the MD simulations both PVF3 and PVF4 have a tendency to shrink from their initially extended state. In Figure 6, we present a series of snapshots of a PVF3 in the course of time. One may notice the quick decay of  $R_g$  in the initial time regime, see Figure 5. Evident are also the fluctuations of  $R_g$  after this time regime, fluctuations which are larger for larger  $G$ . They are due to the very open structure of the PVF, see Figure 6, which allows large displacements of the PVF arms. Such motions

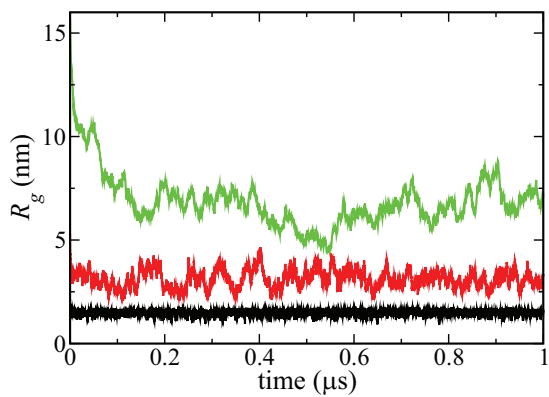


**Figure 5.** Time development of  $R_g$  of PVF with  $G = 2$  (black),  $3$  (red), and  $4$  (green) from below.

lead to large changes in  $R_g$ , even for structures that have long before equilibrated to the given temperature. Moreover, we witness a pronounced interpenetration of the fractal subunits of the PVF, see Figure 6.

From the autocorrelation functions  $C(t)$  related to Figure 5

$$C(t) = \frac{\langle \delta R_g(t) \delta R_g(0) \rangle}{\langle \delta R_g^2 \rangle}, \quad (5)$$

where  $\delta R_g(t) = R_g(t) - \langle R_g \rangle$ ,<sup>[35,37]</sup> we know that the corresponding relaxation times  $\tau_g$  increase much with increasing molecular weight  $N$  (we refrain from displaying here the detailed  $C(t)$  forms). Here, the  $\tau_g$  are defined as the time at which the  $C(t)$  reach the value  $1/e$ . In Table 4, we show for all the PVF considered  $\tau_g$  obtained by averaging over nine individual time intervals covering the whole MD trajectories. For PVF2 and PVF3 the intervals are 100 ns and for PVF4 500 ns long. In Table 4, the corresponding standard

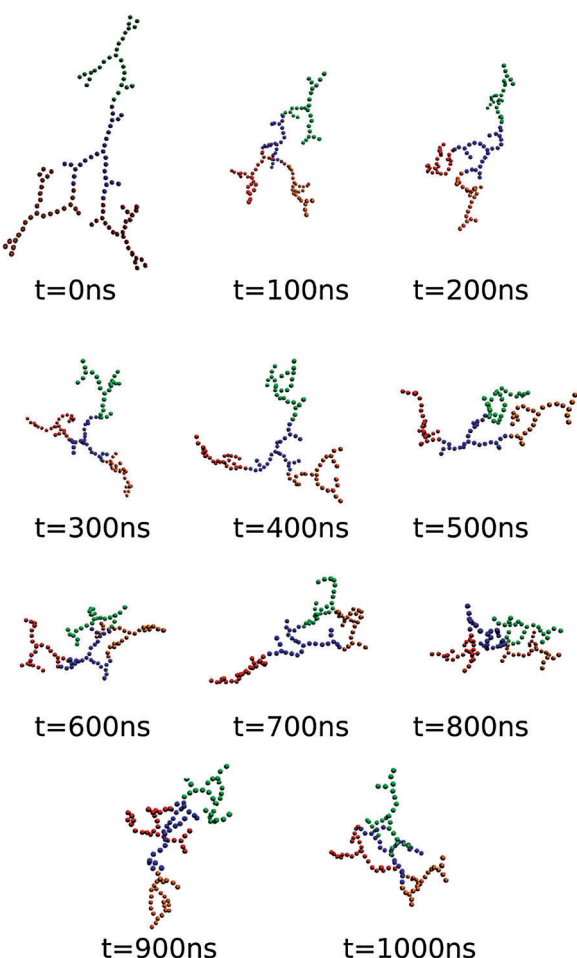


**Figure 6.** Configurations of a PVF of generation  $G = 3$  based on MD simulations. The snapshots are taken at different moments in time. The PVF of generation  $G = 3$  consists of 4 PVF of generation  $G = 2$  which are depicted here in different colors: The central one is blue while the others are red, orange, and green.

**Table 4.** Average values of the relaxation times  $\tau_g$  and  $\tau_{\text{rot}}$  in ns related to the autocorrelation function of the radius of gyration and the rotational correlation functions for PVF and PD of generations two to five as obtained from MD simulations. The presented errors are the standard deviation from the mean.

	PVF		PD	
	$\tau_g$	$\tau_{\text{rot}}$	$\tau_g$	$\tau_{\text{rot}}$
$G = 2$	$0.48 \pm 0.06$	$2.78 \pm 0.08$	$0.33 \pm 0.03$	$2.86 \pm 0.07$
$G = 3$	$5.8 \pm 0.7$	$16.8 \pm 0.5$	$0.76 \pm 0.11$	$6.4 \pm 0.3$
$G = 4$	$58 \pm 5$	$160 \pm 2$	$1.44 \pm 0.20$	$15.2 \pm 1.3$
$G = 5$			$2.31 \pm 0.24$	$33 \pm 3$

deviation from the mean is also shown. We note that all our simulations reach a steady-state within our simulated time scales.

Based on Figure 5 we determined the  $\langle R_g \rangle$  for PVF with  $G = 2, 3$ , and  $4$  as a function of  $N$ , see Table 5 and Figure 7. In doing so, we have not taken into account the region of the fast initial decay (i.e., for PVF2 the first 1 ns, for PVF3

**Table 5.** Average values of the radius of gyration  $\langle R_g \rangle$  in nm for PVF and PD of generations two to five as obtained from MD simulations. For PD the radii of gyration determined by Lee and Larson<sup>[27]</sup> are shown in brackets. All errors are representing the standard deviation of the mean.

	PVF	PD
$G = 2$	$1.5 \pm 0.1$	$1.37 \pm 0.07$
$G = 3$	$3.1 \pm 0.4$	$1.75 \pm 0.07$
$G = 4$	$6.6 \pm 0.8$	$2.15 \pm 0.07$ ( $2.07 \pm 0.1$ )
$G = 5$		$2.60 \pm 0.06$ ( $2.57 \pm 0.2$ )

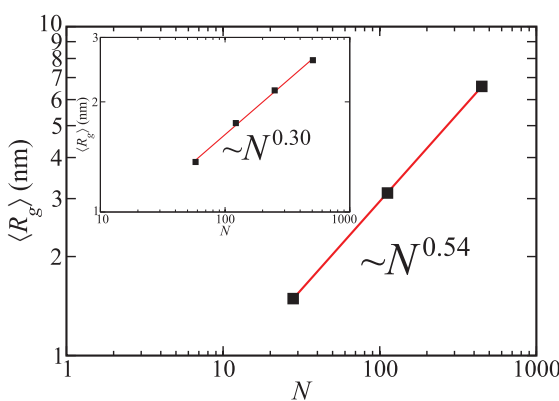


**Figure 7.** The average  $\langle R_g \rangle$  of PVF with  $G = 2, 3$ , and  $4$  as a function of the molecular weight  $N$ . The solid line is a linear fit to the simulation data; the fit implies  $\langle R_g \rangle \sim N^{0.54}$ . The inset shows for the sake of comparison  $\langle R_g \rangle$  for PD of generation two to five, as obtained from our simulations. The corresponding fit to the simulation data implies  $\langle R_g \rangle \sim N^{0.30}$ .

the first 20 ns, and for PVF4 the first 100 ns). As is clearly visible from the double logarithmic plot of Figure 7,  $\langle R_g \rangle$  scales as a power law,  $\langle R_g \rangle \sim N^\gamma$ , with the scaling factor being  $\gamma = 0.54$ . Note that this scaling exponent is somewhat smaller than that found for star polymers, for which one has  $\gamma_{\text{Star}} \approx 0.58$ .<sup>[38,39]</sup> On the other hand, we found  $\gamma_{\text{PD}} = 0.30$  for PD (see the inset of Figure 7), similar to  $\tilde{\gamma}_{\text{PD}} = 1/3$ , as reported from atomistic MD simulations of flexible PD.<sup>[40]</sup> The difference in the  $\gamma$ -exponent for PVF and for PD also renders clear that their compactness differs. As the geometrical realizations suggest (see Figure 2), the PD turn out to be considerably denser than the PVF.

Finally, a rough measure of the shape of polymers is provided by the principal moments  $I_x$ ,  $I_y$ , and  $I_z$  of their gyration tensors (we take  $I_x \leq I_y \leq I_z$ ). The aspect ratios  $I_z/I_x$  and  $I_z/I_y$  for PVF of generations  $G = 2, 3$ , and  $4$  are presented in Figure 8; for all PVF considered they reveal non-spherical shapes. In Figure 8, all presented error bars are based upon the standard deviation from the mean values of  $I_x$ ,  $I_y$ , and  $I_z$ . In contrast, for PD these ratios tend for large  $G$  towards unity,<sup>[28]</sup> which shows that the PD get increasingly spherically symmetric.

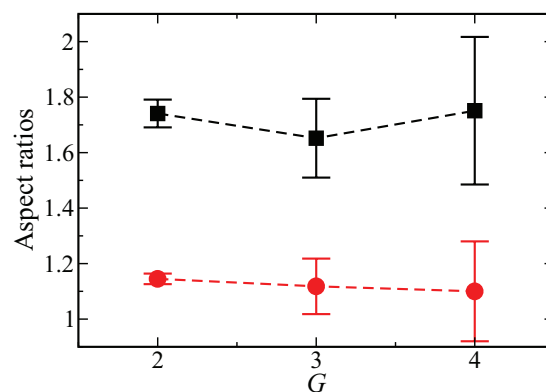


**Figure 8.** Aspect ratios of the principal moments ( $I_x \leq I_y \leq I_z$ ) of the gyration tensor as a function of the generation  $G$ . Shown are the ratios  $I_z/I_y$  (red circles, lower values) and  $I_z/I_x$  (black squares, upper values).

Moreover, for PVF an estimate of the fractal dimension  $d_{\text{frac}}$  can be obtained as follows: First, in the case of a stretched-out PVF embedded in  $2d$  the corresponding fractal dimension  $d_{\text{frac}}^{2d}$  is  $d_{\text{frac}}^{2d} = \ln 4 / \ln 3$ .<sup>[9]</sup> Now, the PVF arms are filamentary and can fold. For a chain the Flory expression is  $\langle R_g \rangle \sim N^{0.6}$ ; here we found for PVF  $\langle R_g \rangle \sim N^{0.54}$ . Using this exponent, we infer for solvated PVF in  $3d$  that  $d_{\text{frac}} \simeq d_{\text{frac}}^{2d} / 0.54 \simeq 2.3$ . This value is quite close to that of a  $2d$  euclidean object, i.e., a simple surface. Moreover, this  $d_{\text{frac}}$  value mirrors the filamentary PVF geometry, namely, the object does not have a clear-cut surface in a topological sense. In contrast, the much more compact PD is almost three dimensional, having a quite well-developed surface, which encompasses the many remaining bulk beads.

### 3.2. Radial Number and Density Profiles

To get a more detailed insight in the structure of PVF, we determine the radial bead distributions and the radial density profiles as a function of the radial distance  $r$  from the COM. At predetermined time steps after the steady-state is reached we evaluate the radial bead distributions using spherical layers of width 0.02 nm and increasing radii centered on the COM, which cover the entire simulation box. In this way, we determine the number of beads within each layer. The mean radial distribution is then obtained by averaging over all the time steps considered. We calculate the corresponding radial bead densities by dividing the obtained bead distributions by the corresponding layer volumes.

For PVF4 we present in Figure 9a the mean radial bead distributions and in Figure 9b the corresponding radial bead densities  $\langle \rho(r) \rangle$ . Based on the previous discussion, the first 100 ns of the MD trajectory are estimated to be the equilibration period for all simulated PVF4, the rest of the trajectory being used to calculate the bead distributions. As can be seen from Figure 9a, the maxima of the bead distributions corresponding to specific shells  $g$  are located at larger  $r$ -values with increasing  $g$ . However, given that the terminal shell  $g = 4$  contains 75% of all PVF beads, the beads of this shell dominate, which results in an extensive broadening of the distribution related to all PVF beads. As can be seen in Figure 9a the corresponding black curve does not show a clear maximum. Moreover, the dominant behavior of the terminal shell is also visible from the fact that the maximum of its bead distribution is located close to the  $\langle R_g \rangle$ -value of the PVF4, see Table 5 and Figure 5. Furthermore, with increasing shell number the PVF arms get to be more flexible, which leads to a significant interpenetration of the different shells, as is evidenced by Figure 9. Consequently, PVF are macromolecules with a rather soft character. This feature allows the solvent to fill very easily the space which is not occupied by PVF beads,

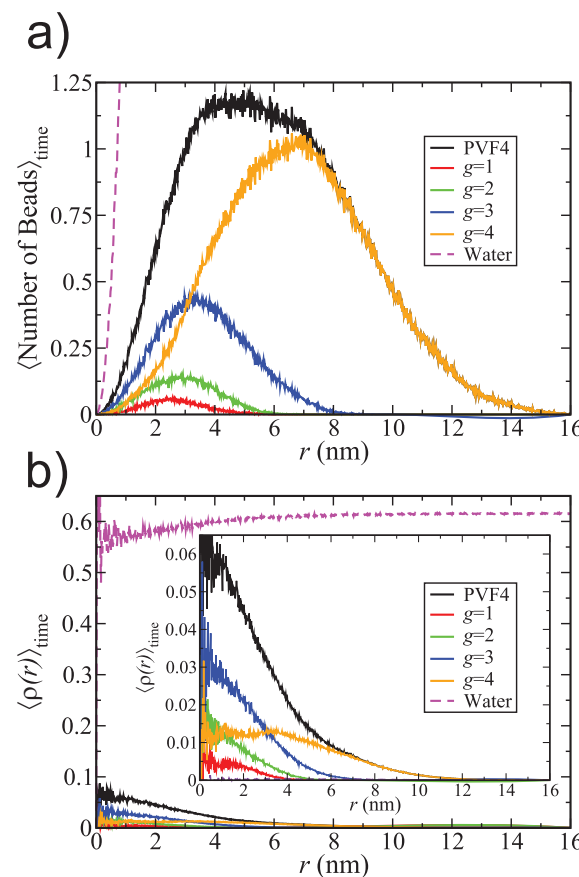


**Figure 9.** (a) Average radial bead distributions and (b) radial bead densities for a PVF4 as a function of the radial distance  $r$  from the COM. Presented are results for all beads of the PVF (black), for the beads from particular shells ( $g = 1$  in red,  $g = 2$  in green,  $g = 3$  in blue, and  $g = 4$  in orange), and for the solvent beads (magenta).

leading to a quite low polymer density for the simulated PVF4 system. Remarkably, neither the specific bead densities nor the water density vanish when approaching the COM of the PVF, see Figure 9b. Hence, contrary to the sketches shown in Figure 2 and 4, the core and the COM of a PVF are located rather far from each other (see Figure 11). Here we have shown only the curves for PVF4; we note, however, that similar findings are also present for the other PVF structures.

In Figure 10a, we display the mean radial bead distributions and in Figure 10b the corresponding radial bead densities  $\langle \rho(r) \rangle$  for PD5. This allows us to compare the radial profiles of PVF4 and PD5. As can be seen in Figure 9 and 10, the width at half maximum for all PVF beads is approximately 7 nm, while for PD it is only around 2 nm. Furthermore, as for PVF4, water penetrates deeply into the PD5. Given that the PVF4 and PD5 systems contain 448 and 506 beads, respectively, this clearly demonstrates that the PVF are less compact than the PD, resulting in a considerable swelling and spatial expansion. Moreover, due

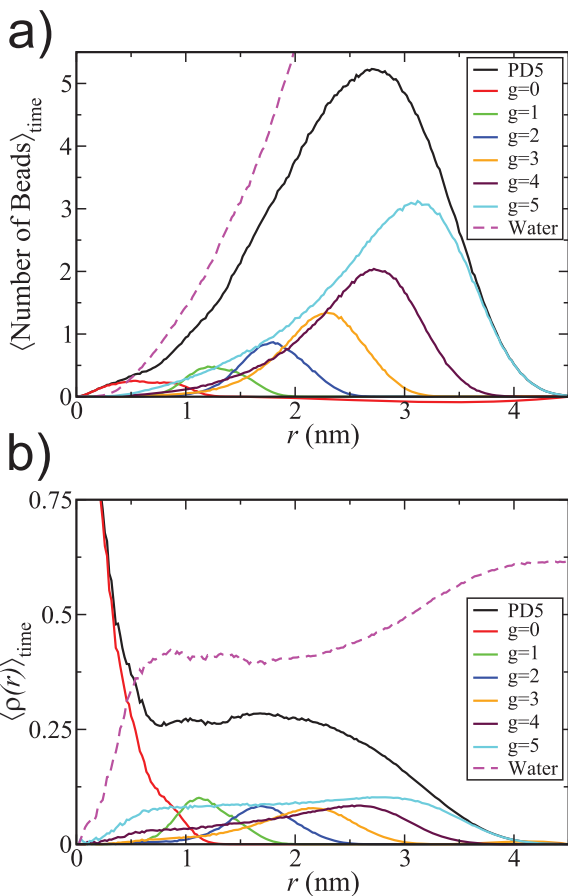


**Figure 10.** (a) Average radial bead distributions and (b) radial bead densities for a PD5 as a function of the radial distance  $r$  from the COM. Presented are results for all beads of the PD (black), for the beads from particular shells ( $g=0$  in red,  $g=1$  in green,  $g=2$  in blue,  $g=3$  in orange,  $g=4$  in maroon, and  $g=5$  in cyan), and for the solvent beads (magenta).

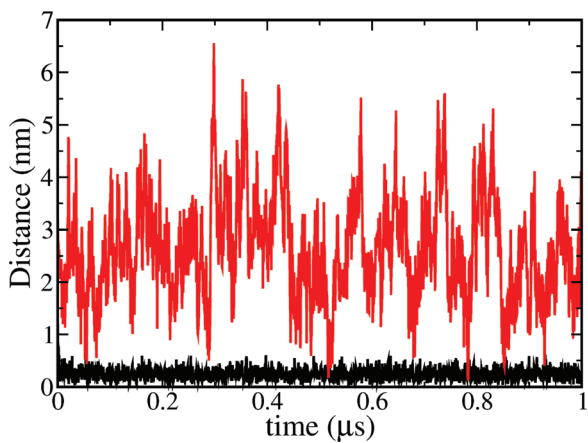


**Figure 11.** Temporal dependency of the distance between the core and the COM of a PD5 (black, lower curve) and of a PVF4 (red, upper curve).

to the dense structure of PD, its core and COM are always rather close, resulting in vanishing densities for all (water and PD) beads which do not belong to the shell  $g = 0$ .

### 3.3. Rotational Autocorrelation Function

The dynamical behavior of the PVF is studied by the rotation of the PVF, which can be described by the rotational autocorrelation function<sup>[35,37,41]</sup>

$$C_{\text{rot}}(t) = \frac{\langle \delta \mathbf{R}_i(t) \cdot \delta \mathbf{R}_i(0) \rangle}{\langle \delta \mathbf{R}_i^2 \rangle}, \quad (6)$$

where  $\delta \mathbf{R}_i(t) = \mathbf{R}_i(t) - \langle \mathbf{R}_i \rangle$ . Furthermore,  $\mathbf{R}_i$  represents the vector from the PVF core bead  $c$  to the peripheral bead  $i$ ,  $\mathbf{R}_i = \mathbf{r}_i - \mathbf{r}_c$ . Hence the average in Equation (6) is performed over all peripheral beads of the PVF. In case of PVF, peripheral beads are beads of functionality one which are connected with the core of the PVF by the longest possible path of PVF beads. Hence a PVF2 has six peripheral beads, while a PVF3 and PVF4 have 12 and 24, respectively. The focus on peripheral beads is justified by the fact that these beads are located most remotely from the core at the very beginning of all simulations (stretched initial configurations) and that the beads of the highest shell are most likely farther away from the core, see the radial density profiles in Figure 9.

In Figure 12, we display  $C_{\text{rot}}(t)$  for PVF2, PVF3, and PVF4 in linear and in the inset in semi-logarithmic scales. As is evident from this representation, none of the correlation functions follow a pure exponential decay, fact indicating multiple relaxation processes. Nevertheless, we proceed in analogy to  $\tau_g$  by setting  $\tau_{\text{rot}}$  to be the time at which the  $C_{\text{rot}}(t)$  reach the value  $1/e$ . In Table 4 we display for all the PVF considered  $\tau_{\text{rot}}$  obtained by averaging over nine individual

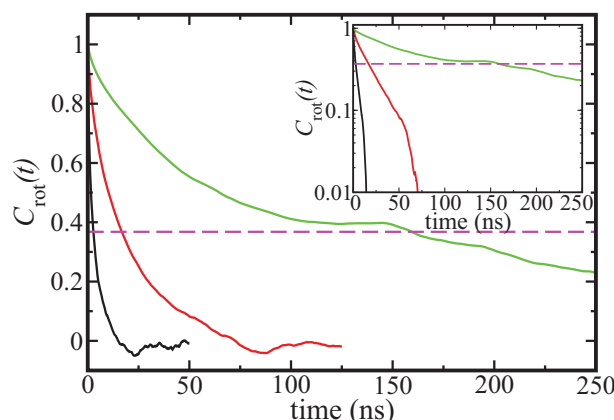


**Figure 12.** Rotational autocorrelation functions of PVF with generations  $G=2$  (black),  $3$  (red), and  $4$  (green) from below. The dashed magenta line represents the equilibration value  $1/e$ . The inset shows the plot in semi-logarithmic scales.

time intervals covering the whole MD trajectories. For PVF2 the intervals are 100 ns long, for PVF3 250 ns, and for PVF4 500 ns. Accordingly, all errors represent the standard deviation from the mean value. As found for  $\tau_g$ ,  $\tau_{\text{rot}}$  increases much with the molecular weight  $N$ . However,  $\tau_{\text{rot}}$  is approximately five and three times larger than  $\tau_g$  for PVF2 and for PVF3 and PVF4, respectively. On the other hand, one finds that  $\tau_g$  is increasing roughly by the factor 10 with growing generation  $G$ , while  $\tau_{\text{rot}}$  increases roughly by the factor 6 and 10, respectively. It is tempting to speculate that these relations imply that both  $\tau_g$  and  $\tau_{\text{rot}}$  scale with  $G$ . However, for a conclusive statement about scaling one needs to investigate more and, especially, larger PVF structures.

For PD it turns out that both relaxation times increasing roughly by the factor 2 with growing  $G$ . Thus, the rotation as a whole (as well as the approach to the steady-state) proceeds much slower for PVF than for PD of comparable molecular weight. This is understandable realizing that for such PVF-PD pairs, the moment of inertia of PVF (which is proportional to  $R_g^2$ ) is much larger than that for PD, a consequence of the spread-out PVF structure. Hence, at the same temperature the object with the larger  $R_g^2$  rotates more slowly.

#### 4. Conclusion

In this work we have studied PAMAM Vicsek fractals (PVF) *in silico* and determined their properties in dilute solutions based on molecular dynamics simulations which employed the coarse-grained MARTINI force-field.<sup>[27]</sup>

Remarkably, the  $R_g$ -values of PVF scale with the molecular weight  $N$ , the scaling exponent turning out to be 0.54, which is considerably larger than the exponents 0.30 determined by us for PD and 0.33 determined for flexible dendrimers in ref.<sup>[40]</sup> We note that the exponent found by us for PVF is rather close but smaller to that found for star polymers.<sup>[38,39]</sup> The observed difference in the scaling exponents implies that with increasing  $N$  the size of PVF increases much more than that of PD. Furthermore, as explicitly shown for a PVF4 we witness strong fluctuations of the radius of gyration  $R_g$ , which lets us conclude that PVF are much softer hyperbranched polymers than the PD (the latter tending to form some sort of dense balls for  $G$  rather large). Moreover, studying the principal moments of the gyration tensor indicates a non-spherical shape for PVF independently of the generation  $G$  while, in contrast, dendrimers with growing  $G$  tend to an increasingly globular shape.<sup>[28]</sup>

In addition to the radius of gyration, we also considered for PVF the radial bead distributions and the radial bead densities as a function of the distance from the center of mass (COM). For PVF we observed a considerable degree of

interpenetration of beads of different shells and that water penetrates it deeply, which leads to a considerable degree of swelling. In contrast, for PD one observes a quite dense geometry accompanied by a significant degree of backfolding of the peripheral shell toward the COM as in ref.<sup>[28]</sup>

Finally, we calculated the rotational autocorrelation functions and obtained the corresponding rotational relaxation times  $\tau_{\text{rot}}$ . As it turned out  $\tau_{\text{rot}}$  increases with growing generation  $G$  roughly by the factors 6 and 10 while for PD the corresponding  $\tau_{\text{rot}}$  increase only roughly by a factor 2, displaying slower rotation of PVF.

This article was devoted to the qualitatively very distinct behavior found in two very important representatives of hyperbranched structures, namely the PD and the PVF. For a more quantitative analysis of PVF, especially when experimental data will become available, full atomistic simulations will be definitely necessary which, however, at the moment go beyond our intentions here.

**Acknowledgements:** The authors acknowledge the use of the computer cluster of the Institute of Macromolecular Compounds RAS and of the Lomonosov supercomputer at the Moscow State University. This work was partly supported by the FP7 Staff Exchange Program (FP7-PEOPLE-2011-IRSES) in the framework of the Project 295302 (SPIDER) and also by the Russian Foundation of Basic Research through Grant No. 14-03-01073 (A.A.G.). Furthermore, the support of the Fonds der Chemischen Industrie and of the Deutsche Forschungsgemeinschaft through Grant No. BI 142/11-1 and through IRTG Soft Matter Science (GRK 1642/1) is gratefully acknowledged.

Received: August 8, 2014; Revised: September 30, 2014; Published online: November 19, 2014; DOI: 10.1002/mats.201400063

**Keywords:** dendrimers; hyperbranched; MARTINI force-field; MD simulations; poly(amidoamine)

- [1] C. Gao, D. Yan, *Prog. Polym. Sci.* **2004**, *29*, 183.
- [2] A. A. Gurtovenko, A. Blumen, *Adv. Polym. Sci.* **2005**, *182*, 171.
- [3] R. La Ferla, *J. Chem. Phys.* **1997**, *106*, 688.
- [4] A. A. Gurtovenko, D. A. Markelov, Y. Y. Gotlib, A. Blumen, *J. Chem. Phys.* **2003**, *119*, 7579.
- [5] J. M. J. Fréchet, *J. Polym. Sci. A: Polym. Chem.* **2003**, *41*, 3713.
- [6] F. Fürstenberg, M. Dolgushev, A. Blumen, *J. Chem. Phys.* **2012**, *136*, 154904.
- [7] A. Kumar, P. Biswas, *J. Chem. Phys.* **2012**, *137*, 124903.
- [8] C. S. Jayanthi, S. Y. Wu, *Phys. Rev. B* **1994**, *50*, 897.
- [9] A. Blumen, C. von Ferber, A. Jurjii, T. Koslowski, *Macromolecules* **2004**, *37*, 638.
- [10] Z. Zhang, S. Zhou, L. Chen, M. Yin, J. Guan, *J. Phys. A: Math. Theor.* **2008**, *41*, 485102.
- [11] A. Jurjii, A. Volta, T. Beu, *Phys. Rev. E* **2011**, *84*, 011801.
- [12] B. Wu, Y. Lin, Z. Zhang, G. Chen, *J. Chem. Phys.* **2012**, *137*, 044903.
- [13] F. Fürstenberg, M. Dolgushev, A. Blumen, *J. Chem. Phys.* **2013**, *138*, 034904.

- [14] P. Biswas, R. Kant, A. Blumen, *Macromol. Theory Simul.* **2000**, *9*, 56.
- [15] R. Kant, P. Biswas, A. Blumen, *Macromol. Theory Simul.* **2000**, *9*, 608.
- [16] P. Biswas, R. Kant, A. Blumen, *J. Chem. Phys.* **2001**, *114*, 2430.
- [17] D. A. Markelov, E. Lähderanta, Y. Y. Gotlib, *Macromol. Theory Simul.* **2010**, *19*, 158.
- [18] M. Dolgushev, G. Berezovska, A. Blumen, *Macromol. Theory Simul.* **2011**, *20*, 621.
- [19] R. W. J. Scott, O. M. Wilson, R. M. Crooks, *J. Phys. Chem. B* **2005**, *109*, 692.
- [20] S. Svenson, D. A. Tomalia, *Adv. Drug Del. Rev.* **2012**, *64*, 102.
- [21] T. J. Prosa, B. B. J. Bauer, E. J. Amis, D. A. Tomalia, R. Scherrenberg, *J. Polym. Sci. Part B: Polym. Phys.* **1997**, *35*, 2913.
- [22] Y. Liu, C. Y. Chen, H. L. Chen, K. Hong, C. Y. Shew, X. Li, L. Liu, Y. B. Melnichenko, G. S. Smith, K. W. Herwig, L. Porcar, W.-R. Chen, *J. Phys. Chem. Lett.* **2010**, *1*, 2020.
- [23] D. Astruc, E. Boisselier, C. Ornelas, *Chem. Rev.* **2010**, *110*, 1857.
- [24] D. A. Markelov, V. V. Matveev, P. Ingman, M. N. Nikolaeva, E. Lähderanta, V. A. Shevelev, N. I. Boiko, *J. Phys. Chem. B* **2010**, *114*, 4159.
- [25] W. D. Tian, Y. Q. Ma, *Chem. Soc. Rev.* **2013**, *42*, 705.
- [26] H. Lee, R. G. Larson, *J. Phys. Chem. B* **2006**, *110*, 18204.
- [27] H. Lee, R. G. Larson, *Macromolecules* **2011**, *44*, 2291.
- [28] K. Karatasos, D. B. Adolf, G. R. Davies, *J. Chem. Phys.* **2001**, *115*, 5310.
- [29] D. A. Markelov, S. V. Lyulin, Y. Y. Gotlib, A. V. Lyulin, V. V. Matveev, E. Lähderanta, A. A. Darinskii, *J. Chem. Phys.* **2009**, *130*, 044907.
- [30] S. J. Marrink, H. J. Risselada, S. Yefimov, D. P. Tieleman, A. H. de Vries, *J. Phys. Chem. B* **2007**, *111*, 7812.
- [31] T. Vicsek, "Fractal Growth Phenomena", World Scientific, Singapore **1992**.
- [32] C. J. Hawker, R. Lee, J. M. J. Fréchet, *J. Am. Chem. Soc.* **1991**, *113*, 4583.
- [33] D. Hölder, A. Burgath, H. Frey, *Acta Polym.* **1997**, *48*, 30.
- [34] S. J. Marrink, D. P. Tieleman, *Chem. Soc. Rev.* **2013**, *42*, 6801.
- [35] B. Hess, C. Kutzner, D. Van Der Spoel, E. Lindahl, *J. Chem. Theory Comput.* **2008**, *4*, 435.
- [36] H. J. C. Berendsen, J. P. M. Postma, W. F. van Gunsteren, A. R. H. J. DiNola, J. R. Haak, *J. Chem. Phys.* **1984**, *81*, 3684.
- [37] M. P. Allen, D. J. Tildesley, "Computer Simulation of Liquids", Clarendon Press, Oxford **1987**.
- [38] H. P. Hsu, W. Nadler, P. Grassberger, *Macromolecules* **2004**, *37*, 4658.
- [39] M. M. Nardai, G. Zifferer, *J. Chem. Phys.* **2009**, *131*, 124903.
- [40] P. K. Maiti, B. Bagchi, *J. Chem. Phys.* **2009**, *131*, 214901.
- [41] S. V. Lyulin, A. A. Darinskii, A. V. Lyulin, M. A. J. Michels, *Macromolecules* **2004**, *37*, 4676.